The transcription factor Pdr802 regulates Titan cell formation, quorum sensing, and pathogenicity of *Cryptococcus neoformans*

Julia C. V. Reuwsaat[1,2], Daniel P. Agustinho[2], Heryk Motta[1], Holly Brown[2], Andrew L. Chang[2], Michael R. Brent[3], Livia Kmetzsch[1,4,5], and Tamara L. Doering[2,5].

[1]Molecular Biology of Pathogens Laboratory, Biotechnology Center, Universidade Federal do Rio Grande do Sul, Porto Alegre, Brazil.

[2]Department of Molecular Microbiology, Washington University School of Medicine, St. Louis, Missouri, USA.

[3]Center for Genome Sciences and Systems Biology, Washington University School of Medicine, and Departments of Computer Science and Genetics, Washington University, St. Louis, Missouri, USA.

[4]Department of Molecular Biology and Biotechnology, Universidade Federal do Rio Grande do Sul, Porto Alegre, Brazil.

[5]Corresponding authors: livia.kmetzsch@ufrgs.br, doering@wustl.edu

Running head: The role of Pdr802 in *Cryptococcus neoformans* virulence.

1

ABSTRACT

Cryptococcus neoformans is a ubiquitous, opportunistic fungal pathogen that kills almost 200,000 people worldwide each year. It is acquired when mammalian hosts inhale the infectious propagules; these are deposited in the lung and, in the context of immunocompromise, may disseminate to the brain and cause lethal meningoencephalitis. Once inside the host, *C. neoformans* undergoes a variety of adaptive processes, including secretion of virulence factors, expansion of a polysaccharide capsule that impedes phagocytosis, and the production of giant (Titan) cells. The transcription factor Pdr802 is one regulator of these responses to the host environment. Expression of the corresponding gene is highly induced under host-like conditions *in vitro* and is critical for *C. neoformans* dissemination and virulence in a mouse model of infection. Direct targets of Pdr802 include the quorum sensing proteins Pqp1, Opt1 and Liv3; the transcription factors Stb4, Zfc3 and Bzp4, which regulate cryptococcal brain infectivity and capsule thickness; the calcineurin targets Had1 and Crz1, important for cell wall remodeling and *C. neoformans* virulence; and additional genes related to resistance to host temperature and oxidative stress, and to urease activity. Notably, cryptococci engineered to lack Pdr802 showed a dramatic increase in Titan cells, which are not phagocytosed and have diminished ability to directly cross biological barriers. This explains the limited dissemination of *pdr802* mutant cells to the central nervous system and the consequently reduced virulence of this strain. The role of Pdr802 as a negative regulator of Titan cell formation is thus critical for cryptococcal pathogenicity.

IMPORTANCE

The pathogenic yeast *Cryptococcus neoformans* presents a worldwide threat to human health, especially in the context of immunocompromise, and current antifungal therapy is hindered by cost, limited availability, and inadequate efficacy. After the infectious particle is inhaled, *C. neoformans* initiates a complex transcriptional program that integrates cellular responses and enables adaptation to the host lung environment. Here we describe the role of the transcription factor Pdr802 in the response to host conditions and its impact on *C. neoformans* virulence. We identified direct targets of Pdr802 and also discovered that it regulates cellular features that influence movement of this pathogen from the lung to the brain, where it causes fatal disease. These findings advance our understanding of a serious disease.

INTRODUCTION

Cryptococcosis is a fungal infection caused by *Cryptococcus neoformans* and *Cryptococcus gattii. C. neoformans* is a ubiquitous opportunistic pathogen that infects mainly immunocompromised patients, while *C. gattii* is capable of infecting immunocompetent individuals (1). Cryptococcosis causes 180,000 deaths worldwide each year, including roughly 15% of all AIDS-related deaths (2), and is initiated by the inhalation of spores or desiccated yeast cells. In immunocompetent individuals, this typically leads to an asymptomatic pulmonary infection that is controlled by the host immune response, although a population of *C. neoformans* may remain latent for extended periods of time (3–5).

3

44   Under conditions of immunocompromise, cryptococci disseminate from the lung to

45   the brain. Mechanisms that have been suggested to mediate fungal crossing of the

46   blood-brain barrier (BBB) include transcellular migration, in which the yeast cells enter

47   and exit vascular endothelial cells (6–9); paracellular movement, in which they cross the

48   BBB at junctions between endothelial cells (10–12); and 'Trojan horse' crossing, whereby

49   macrophages harboring *C. neoformans* enter the brain (13). Cryptococcal

50   meningoencephalitis is difficult to treat and frequently lethal, for reasons that include the

51   availability and cost of therapy (14, 15).

52   The ability of *C. neoformans* to survive and proliferate in the lung, and

53   subsequently disseminate to the brain, depends on viability at mammalian body

54   temperature and the expression of multiple virulence traits; these include secreted factors

55   (16, 17), a polysaccharide capsule that surrounds the cell wall (18), and the production of

56   giant (Titan) cells (19, 20). One secreted molecule, the pigment melanin, associates with

57   the cell wall, where its antioxidant properties protect fungal cells from reactive oxygen

58   species produced as a host immune defense (21–25). Urease, a secreted metalloenzyme

59   that converts urea to ammonia and CO_2, may affect the course of infection by modulating

60   environmental pH and damaging host tissue structure (11, 12, 26).

61   The capsule, composed primarily of large polysaccharides (27–29), is a key

62   cryptococcal virulence factor that impairs phagocytosis by immune cells (30–35). This

63   dynamic entity changes its size and structure during interactions with the host or external

64   environment (36–39), contributing to fungal adaptation (40, 41). Capsule polysaccharides

65   that are shed from the cell enable diagnosis of cryptococcal infection and also impede

66   host responses (35, 42).

67 Titan cells display a cryptococcal morphotype that has been variously

68 characterized as having cell body diameter (excluding the capsule) greater than 10 or 15

69 μm or total cell diameter (including the capsule) that exceeds 30 μm (20, 43, 44). These

70 cells are polyploid and produce normal-size cells during infection (19, 45, 46). Titan cell

71 formation is triggered by exposure to the host environment, including nutrient starvation,

72 reduced pH, and hypoxia (47–49), although the extent of induction depends on the host

73 immune response and the duration of infection (45, 50). Titan cell production appears to

74 benefit the development of pulmonary *C. neoformans* infection, since these large cells

75 are less susceptible to internalization by host phagocytes and more resistant to oxidative

76 stress than normal-size cells (19, 46). Some of these effects may be explained by the

77 highly cross-linked capsule and thickened cell wall of Titan cells (51). In contrast to their

78 success in the lungs, Titan cells show impaired dissemination to the brain (19, 46).

79 *C. neoformans* experiences a dramatic change in conditions upon entering a host,

80 including altered nutrient levels and pH. To adapt to the new environment, cryptococci

81 activate a network of transcription factors (TFs) (39, 52). For example, imbalances in ion

82 homeostasis trigger transcriptional changes mediated by the TFs Zap1 (53), Cuf1 (54),

83 Pho4 (55), Cir1 (56), and Crz1 (57). Alkaline pH stimulates expression of the TF Rim101,

84 which enables growth under basic conditions and other stresses such as high salt and

85 iron limitation; it also promotes the association of capsule polysaccharide with the cell

86 and the formation of Titan cells (47, 58).

87 Overlapping TF circuits regulate cryptococcal virulence determinants, including

88 polysaccharide capsule production and melanin synthesis. For example, Usv101, an

89 important regulator of capsule thickness and polysaccharide shedding, also regulates

90   three other TFs (Gat201, Crz1, and Rim101) and multiple polysaccharide-related

91   enzymes (59). Gat201 further regulates additional virulence-related transcription factors

92   and the anti-phagocytic protein Blp1 (60), while Crz1 plays a central role in the

93   maintenance of plasma membrane and cell wall stability (57, 61, 62). Crz1 expression is

94   also modulated by the calcineurin signaling pathway, which is required for normal yeast

95   growth at 37°C, virulence, and sexual reproduction (63). A group of TFs, including

96   Usv101, Bzp4, Hob1, and Mbs1 (59, 64), act together to regulate melanin production;

97   deletion of Bzp4 also alters capsule (52).

98   In this study, we investigated the TF Pdr802. The corresponding gene has a high

99   rate of non-synonymous mutations, which suggests it is evolving rapidly (65). Pdr802 has

100   previously been implicated in *C. neoformans* virulence (39, 52, 66), but its specific role

101   and targets are not known. We discovered that Pdr802 is induced in host-like conditions,

102   is a negative regulator of Titan cell formation, and influences capsule thickness and

103   phagocytosis by macrophages. It also regulates genes whose products act in cell wall

104   remodeling, virulence factor production, resistance to host temperature and oxidative

105   stress, and quorum sensing. These functions make Pdr802 critical for cryptococcal

106   survival in the lung and dissemination to the brain.

107

108   **RESULTS**

109   **The role of Pdr802 in *C. neoformans* virulence**

110   The importance of Pdr802 in *C. neoformans* virulence has been demonstrated in

111   multiple experimental models. Liu and collaborators first reported in 2008 that partial

112   deletion of *PDR802* reduced *C. neoformans* infectivity in a competition assay of pooled

6

113   *C. neoformans* strains (66). In 2015, Maier *et al* showed that a *pdr802* deletion mutant

114   had reduced virulence when tested individually in a short-term mouse model of infection

115   (39). Later that year, Jung and colleagues reported that Pdr802 was required for full

116   virulence in both wax moth larvae and short-term mouse infection using pooled strains

117   (52). Most recently, Lee and collaborators showed that Pdr802 was required for brain

118   infection (67).

119   To further investigate the role of Pdr802 in pathogenesis, we complemented a

120   complete deletion strain in the KN99α background that we had previously generated

121   (*pdr802*) (39) with the intact gene at its native locus (*PDR802*). To examine targets of

122   Pdr802, we also constructed a strain that expresses the protein fused to mCherry at its

123   N-terminus (Figure S1A). All of these strains lacked or expressed RNA encoding *PDR802*

124   or its modified forms as expected (Figure S1B) and *PDR802* was expressed at wild-type

125   levels in the complemented and modified strains (Figure S1C).

126   We next assessed the long-term survival of C57BL/6 mice infected with the

127   parental wild-type strain (KN99α), the deletion mutant (*pdr802*), or the complemented

128   mutant (*PDR802*). In this model, mice infected with the parent or complemented strains

129   survived for roughly three weeks, while those infected with the deletion mutant showed a

130   striking increase in survival: all animals survived for at least 65 days and over half

131   survived to the end of the study (100 days; Figure 1A). The lung burden measured at the

132   time of death for *pdr802*-infected mice in this study was approximately 100-fold lower

133   than that of wild type infections (Figure S2A), demonstrating the importance of this TF in

134   *C. neoformans* virulence. Mean brain burden at the time of death was more similar

135   between mutant and wild type infections (Figure S2A), although we did note some

136   heterogeneity in this measure for *pdr802*-infected mice; animals sacrificed at around two

137   months of infection (red symbols) showed brain burden similar to WT levels, while brain

138   burden of mice sacrificed at day 100 (blue symbols) ranged between zero fungal cells

139   and WT level.

140   We next examined the time course of fungal proliferation in the lungs. As

141   expected, the burdens of WT and the complemented mutant strains increased steadily

142   over an 18-day interval (Figure 1B), eventually reaching roughly 10^5 times the original

143   inoculum. Towards the end of this period, these cells were also detected in the blood and

144   brain (Figure S2B). In contrast, the lung burden of *pdr802* remained close to the inoculum

145   throughout this period, with no mutant cells detected in the blood or brain. At a late time

146   point of *pdr802* infection (75 days), we again noted some heterogeneity of fungal burden:

147   one mouse had high lung burden with no dissemination, another had high lung burden

148   with moderate brain burden, and the third had extremely low lung burden with no

149   dissemination (Figure S2C). No colony-forming units (CFU) were detected in the blood of

150   *pdr802*-infected mice at any point during infection. These results suggest that even

151   though the *pdr802* mutant is generally hypovirulent and remains at low levels in the lung,

152   it can occasionally reach the brain and, given enough time, accumulate there (see

153   Discussion).

154   Given the dramatic effects of Pdr802 on fungal virulence, we wondered about the

155   specific biological processes in which this transcription factor is involved. We first

156   examined the behavior of the *pdr802* strain *in vitro*, including stress conditions that might

157   be encountered in the host. We saw no differences in growth of the mutant compared to

158   WT cells under conditions that challenge cell or cell wall integrity, including the presence

159   of sorbitol, high salt, cell wall dyes, caffeine, sodium dodecyl sulfate (SDS), or ethanol

160   (Figure S3A-C). The mutant also showed no altered susceptibility to elements of the host

161   response, such as nitrosative or oxidative stresses, or in melanin production. All of these

162   results held whether growth was at 30°C, 37°C, or 37°C in the presence of 5% CO_2,

163   which was recently described as an independent stress for *C. neoformans* (68) (Figure

164   S3A-C). Finally, the mutant showed no difference from wild-type cells in secretion of

165   urease at 30°C or 37°C (Figure S3D).

Pdr802 is regulated by "host-like" conditions

167   We next tested the growth of the *pdr802* mutant under conditions more like those

168   encountered inside the mammalian host, using tissue culture medium (DMEM) at 37°C in

169   the presence of 5% CO_2. We found that although the *pdr802* mutant grew like WT in rich

170   medium (YPD), it grew poorly in DMEM (Figure S4A-B). To test whether the mutant cells

171   were dead or just static after growth in DMEM, we plated aliquots on solid medium to

172   measure CFU over time (Figure 2A). The *pdr802* culture showed a dramatic decrease in

173   viability compared to WT and the complemented strain, which was greatest in the first 24

174   h. This is the same time frame in which expression of the *PDR802* gene shows a striking

175   increase in wild type cells, as measured by RNA-Seq (Figure 2B).

176   Another important feature that is induced by growth in DMEM at 37°C and 5% CO_2

177   is the polysaccharide capsule, which we previously reported to be regulated by Pdr802,

178   based on negative staining with India ink (39). Fluorescence microscopy confirmed

179   increased capsule thickness of the mutant, which reverted to WT in the complemented

180   strain (Figure 3A). To quantify this change, we took advantage of a semi-automated

181   assay that we have developed (Figure S5), which measures capsules on a population

182   scale (Figure 3B) and is therefore very sensitive. This analysis showed that the capsule

183   thickness of *pdr802* cells resembles that of the well-studied hypercapsular mutant *pkr1*

184   (39, 69, 70) and is completely restored to WT by complementation at the native locus

185   (Figure 3C). Previous studies suggest that capsule thickness upon induction reflects the

186   size of the dominant capsule polymer (glucuronoxylomannan; GXM) (71, 72), which can

187   be analyzed by agarose gel migration and blotting with anti-capsule antibodies (71).

188   Consistent with the difference we observed in capsule thickness by imaging, this method

189   showed decreased mobility of GXM from *pdr802* as capsule induction progressed (Figure

190   S4C).

191   To validate the observations that we had made in standard 'host-like' conditions

192   based on synthetic tissue culture medium, we conducted similar studies in mouse serum

193   at 37°C and 5% CO_2. These conditions induced an even more pronounced hypercapsular

194   phenotype of the *pdr802* mutant (Figures 4A and 4B), as well as reduced cell viability

195   (Figure 4C) and increased cell body diameter (Figure 4D).

196   We were intrigued by the enlarged cell body and capsule of the *pdr802* mutant

197   cells in host-like conditions *in vitro* and decided to examine these phenotypes *in vivo*. For

198   these studies, we isolated fungal cells from the lungs of mice at various times after

199   infection and assessed their morphology by negative staining (Figure 5A). At each time

200   point, the mean mutant cell body diameter was larger than that of the controls.

201   Additionally, while this parameter was stable for WT and complemented strains

202   throughout the infection period, it trended larger at the end of the infection period for the

203   deletion mutant (Figure 5B). In contrast, mutant capsule thickness, although initially

204   larger than that of control cells, changed little throughout the period, while capsule

205   thickness of control cells increased to that level or beyond (Figure 5C). Furthermore,

206   although the total cell diameter of *pdr802* cells consistently exceeded that of WT and

207   complemented cells, their sizes became more comparable late in infection (Figure S6A).

208   Over time, therefore, the ratio of total cell diameter to cell body diameter for WT and

209   *PDR802* cells steadily increased, while it remained roughly constant for the mutant

210   (Figure S6B).

Pdr802 negatively regulates Titan cell formation

212   We were particularly interested in the cell size phenotype of *pdr802* because Titan

213   cells have been strongly implicated in cryptococcal pathogenesis (19). By any definition

214   of this morphotype (cell body diameter greater than 10 or 15 µm or total cell diameter

215   greater than 30 µm), our mutant cell populations were dramatically enriched in Titan cells

216   at every time of infection that we assessed (Figure S6C).

217   To specifically test Titan cell formation by the *pdr802* strain, we subjected mutant

218   cells to *in vitro* conditions that induce this process (49) and analyzed the resulting

219   population by flow cytometry. Consistent with our *in vivo* observations, Titan cells

220   constituted a much larger fraction of the population in the mutant culture (13.2%) than in

221   the WT and complemented cultures (1.62% and 1.40%, respectively) (Figure 6).

222   Titan cells are poorly engulfed by host phagocytes (19, 45, 73), which may reflect

223   their increased size as well as alterations in capsule and cell wall (51). We observed this

224   reduced uptake for all strains after growth in conditions that favor Titan cell formation

225   (Figure 7, Titan vs YPD). Also, all strains showed a reduction in phagocytosis after

226   capsule induction in DMEM (Figure 7, DMEM vs YPD), which is not surprising because

11

227   the capsule is antiphagocytic (31, 73). Notably, the reduction in uptake was greatest for

228   the *pdr802* mutant in both of these conditions, even though it showed normal engulfment

229   when all strains were grown in the control condition (YPD). This is likely because the

230   mutant culture is both hypercapsular and enriched in Titan cells.

231   **Identification of direct, functional targets of Pdr802**

232   To identify direct targets of Pdr802, we performed chromatin immunoprecipitation

233   followed by sequencing (ChIP-Seq). We then compared the DNA sequences

234   immunoprecipitated by anti-mCherry mAb from cells expressing mCherry-Pdr802, which

235   grow similarly to WT (Figure S7A), and untagged cells. Both strains were grown for 24

236   hours in DMEM at 37°C and 5% CO_2, as this condition induces *PDR802* expression

237   dramatically compared to standard YPD growth conditions (Figure 2B).

238   Using 2-fold-enrichment over control as a cutoff value for peaks with adjusted p

239   value <0.05, we identified 656 binding sites for mCherry-Pdr802 in genomic DNA. Of

240   these, 540 occurred within 1,000 bp upstream of transcription start sites (Data Set S1,

241   Sheets 1 and 2), which we used as an approximation of regulatory regions. Application of

242   Discriminative Regular Expression Motif Elicitation (DREME) (74) to this set of upstream

243   regions identified several putative Pdr802 binding motifs, which were highly enriched in

244   GA (TC) (Figure S7B). Notably, the ChIP-seq data also suggested self-regulation of

245   *PDR802*, as has been reported for other cryptococcal TFs (75, 76) (Figure S7C).

246   To complement our ChIP studies, we determined the set of genes regulated by

247   Pdr802 under host-like conditions by performing RNA-Seq of WT and *pdr802* cells after

248   growth for 24 h in DMEM at 37°C and 5% CO_2 (Data set 1, Sheet 3). We then used dual-

249   threshold optimization (DTO) to analyze the RNA-seq and ChIP-seq data sets together.

250   This statistical method allowed us to combine the evidence from binding and expression

251   studies to converge on a set of direct and functional TF targets (77). The Pdr802 target

252   genes yielded by this analysis include key players in multiple processes implicated in

253   cryptococcal virulence, including quorum sensing, Titan cell formation, and stress

254   resistance (Data set 1, Sheets 4 and 5).

255   **Pdr802 represses Titan cell production through regulation of quorum sensing**

256   **proteins**

257   The most striking phenotype we observed in cells lacking *PDR802* is the marked

258   increase in Titan cell formation. We therefore examined our DTO target list for genes

259   known to influence this phenotype, such as those involved in quorum sensing. Recent

260   studies have shown that the quorum sensing peptide Qsp1 is a negative regulator of

261   Titan cell formation (47, 48); Titan cell formation increases upon deletion of the gene

262   encoding this peptide (*QSP1*) or proteins that mediate its maturation and import (*PQP1*

263   and *OPT1*, respectively). We found that Pdr802 positively regulates *PQP1* and *OPT1*

264   gene expression (Table 1), consistent with its repression of Titan cell formation.

265   A study of *C. neoformans* cells exposed to Titan cell inducing conditions *in vitro*

266   reported that 562 genes were upregulated in this condition, while 421 genes were

267   downregulated (48). The overlap of these genes with our DTO set of Pdr802-regulated

268   genes included three TF genes *LIV3*, *STB4*, and *ZFC3* (48) (Data Set S2, Sheets 1 and

269   2). The first two are repressed during Titan cell induction while *ZFC3* (also known as

270   *CQS2*) is induced. Our analysis showed that Pdr802 positively regulates expression of

271   *LIV3* and *STB4*, while it negatively regulates *ZFC3* (Table 1), in concordance with our

13

272   phenotypic observations of Titan cell formation. Notably, Liv3 and Zfc3 are responsive to

273   the peptide Qsp1 (75, 76) and are important for *C. neoformans* virulence, while Stb4

274   influences cryptococcal brain infection (67).

275   **Pdr802 coordinates cryptococcal response to the host environment**

276   *C. neoformans* deploys a variety of proteins to resist the many challenges it

277   experiences upon host entry, which include oxidative and temperature stress. Multiple

278   genes that are central to these responses were identified as direct, functional targets of

279   Pdr802 by our DTO analysis (Table 2). For example, Pdr802 induces the expression of

280   genes whose products detoxify reactive oxygen species (ROS), such as *CAT1*, *CAT2*,

281   and *SOD1* (78, 79), or participate in resistance to these compounds, such as *FZC34*,

282   *MIG1*, and *CCK1* (52, 80, 81) (Table 2). Both the kinase Cck1 (also known as Yck2) and

283   the TF Fzc34 have been implicated in cryptococcal virulence (80, 82).

284   As noted above, melanin has important anti-oxidant properties that promote

285   cryptococcal survival inside the host (16). Under host-like conditions, Pdr802 regulates

286   genes required for melanization, even though it melanizes normally *in vitro*. These genes

287   include *CAC1*, *PKC1*, *CUF1*, and *SNF5* (Table 2). Cac1 is an adenylyl cyclase

288   responsible for cyclic AMP (cAMP) production in *C. neoformans*, which plays a central

289   role in melanin synthesis as well as proper capsule production, mating and virulence (83).

290   The kinase Pkc1 induces production of the laccase (Lac1) that forms melanin and plays a

291   key role in resistance to oxidative and nitrosative stress (84, 85); the TF Cuf1 regulates

292   *LAC1* expression and is important for cryptococcal virulence (86, 87); and *SNF5* is

293   required for full melanization (88). Melanin occurs in the fungal cell wall, which is another

294   key component in fungal stress resistance. Pdr802 is also a direct, functional regulator of

14

295   several genes whose products influence cell wall glycan content: two chitin deacetylases

296   (Cda3 and Mp98) and the mannoprotein MP88 (Table 2). Changes in mannose and chitin

297   occur in Titan cell walls (51).

298   Pdr802 positively regulates the expression of several proteins required for yeast

299   growth at 37ºC, including the kinases Kic1 and Ire1 (Table 2). Ire1 is a regulator of the

300   cryptococcal Unfolded Protein Response (UPR) pathway and lack of Ire1 or Kic1 impacts

301   *C. neoformans* virulence (80, 89). Pdr802 also modulates cryptococcal urease activity,

302   which is required for dissemination to the central nervous system (CNS) (11, 12), by

303   regulating the urea transporter Dur3 and other proteins that influence urease activity (e.g.

304   the kinases Fab1, Kin1, and Gut1 and the TF Hlh1) (Table 2). Deletion of *FAB1*, *KIN1*, or

305   *HLH1* impair urease activity in *C. neoformans*, while *GUT1* disruption induces it (52, 80).

306   Above we documented the role of Pdr802 in capsule synthesis, which is

307   dramatically upregulated in the host environment in general and is further increased in

308   cells lacking this TF. We found that Pdr802 is a positive regulator of multiple genes that

309   have been implicated in reducing cryptococcal capsule thickness. These include the

310   kinases Arg2, Iks1, and Ksp1; the TF Fzc51; and the phosphodiesterase Pde2 (Table 2).

311   Notably, null mutants for those genes are hypercapsular, similar to *pdr802* cells (52, 80,

312   90). Pdr802 is a negative regulator of the TF Bzp4, which, as mentioned above, positively

313   regulates capsule (Table 2) (52).

Pdr802 regulates calcineurin target genes

315   The calcineurin signaling pathway is activated by calcium and governs stress

316   response and virulence in *C. neoformans* (91–93). One major mediator of calcineurin

15

317   signaling is the transcription factor Crz1 mentioned above, which is highly responsive to

318   temperature and influences cryptococcal virulence (57, 62). Upon intracellular calcium

319   influx calcineurin dephosphorylates Crz1, which then translocates to the nucleus and

320   regulates gene expression (57, 63). We found that Pdr802 binds the *CRZ1* gene

321   promoter and positively regulates its expression (Figure 8A, Table 2, and Data Set S2,

322   Sheet 3). Pdr802 also binds and regulates five other genes whose products are

323   dephosphorylated by calcineurin; these include the phosphatase Had1, which is

324   important for cryptococcal cell wall remodeling and virulence (Figure 8B, Table 2, and

325   Data Set S2, Sheet 3) (63, 94).

326   Because Crz1 helps maintain normal cryptococcal Ca^{2+} concentrations through the

327   regulation of calcium transporters (57), we wondered about the intracellular calcium

328   levels in *pdr802* cells. We found that after 24 hours of growth in DMEM, the level of

329   cytosolic calcium in the mutant significantly exceeded that of WT or complemented

330   strains (Figure 8C). It was still, however, below that of a *crz1* null mutant, supporting that

331   Pdr802 is not the sole regulator of *CRZ1* expression. Notably, *PDR802* deletion had no

332   effect in rich medium (YPD), which reinforces our hypothesis that Pdr802 acts primarily in

333   host-like conditions. To further explore the relationship of Pdr802 and calcineurin, we

334   compared published gene expression profiles of a calcineurin mutant (57) to our DTO

335   data set. Of the 393 genes that are differently expressed in the calcineurin mutant under

336   thermal stress, 26 are regulated by Pdr802 (Data Set S2, Sheet 4).

337

338   **DISCUSSION**

16

339   We have shown that Pdr802 is a potent regulator of cryptococcal responses to the

340   host environment. In this context, it influences the formation of capsule and Titan cells as

341   well as cellular responses to temperature and oxidative stress, acts as a downstream

342   effector of calcineurin, and modulates calcium availability. The last function is likely

343   achieved through its positive regulation of the transcription factor Crz1, which in turn

344   modulates the calcium transporters Pmc1 and Vcx1 (57). Since calcium ion is a major

345   second messenger in eukaryotic cells, its accumulation in *pdr802* cells affects multiple

346   processes central to host interactions, including stress responses, cell wall integrity, and

347   capsule size (61, 62, 92, 95, 96).

348   *C. neoformans* dissemination to the brain is the main driver of patient mortality (2).

349   We found that dissemination of *pdr802* cells is significantly impaired, although they do

350   occasionally reach the brain. These observations can be explained by a combination of

351   factors. First, the limited accumulation of the *pdr802* mutant in the lungs, due to factors

352   summarized above, may directly affect dissemination (97). Second, this strain survives

353   poorly in mouse serum, as demonstrated directly by our culture experiments and

354   indirectly by our inability to detect it in the blood of infected mice, even 75 days after

355   infection. The latter might be because the cells do not reach the blood or because they

356   are rapidly eliminated, consistent with previous observations (98). Third, the thick

357   capsules of the *pdr802* mutant reduce its ability to reach the brain. This is true whether

358   fungal entry occurs directly, by the movement of free fungi across the BBB, or indirectly,

359   via a Trojan horse mechanism that requires macrophage uptake (99); such uptake is

360   impeded by enlarged capsules, independent of cell size (31). Fourth, calcium imbalance

361   directly affects cryptococcal transmigration (100). Finally, *pdr802* cells show reduced

362   expression of genes required for urease activity, which promotes *C. neoformans*

17

363   dissemination to the CNS (11, 12, 100). Interestingly, despite all of these obstacles to

364   dissemination, mutant cells that do reach the brain are able to proliferate to wild-type

365   levels.

366   Titan cells are a robust and persistent morphotype of *C. neoformans* that

367   contributes to yeast virulence (45). We showed that cells lacking Pdr802 demonstrate

368   increased formation of Titan cells *in vivo* and *in vitro*, suggesting that this TF is a novel

369   repressor of this process. Although Titan cells enhance aspects of cryptococcal

370   pathogenesis (19, 101), their overproduction negatively impacts dissemination to the

371   brain due to their resistance to phagocytosis by macrophages (19, 45) and decreased

372   penetration of biological barriers (19).

373   Our combined analysis of DNA binding and gene expression data allows us to

374   understand the increase in Titan cell formation that occurs upon deletion of *PDR802*.

375   Under host-like conditions, Pdr802 positively regulates Pqp1, Opt1 and Liv3, all key

376   proteins in the cryptococcal quorum sensing pathway, which represses Titan cell

377   formation (47, 48). In the absence of this TF, quorum sensing is impaired, increasing

378   Titan cell formation. Pdr802 may also indirectly modulate Titan cell formation by

379   regulating other TFs that impact this process, such as Zfc3 (Cqs2) and Stb4.

380   We know that capsule, a key virulence factor, is typically highly induced in the host

381   or host-like conditions (102). Our studies *in vitro*, *ex vivo*, and *in vivo* show that Pdr802

382   normally reins in this process. This likely occurs via a combination of Pdr802's repression

383   of the TF Bzp4, which positively regulates capsule size, and the induction of other factors

384   (e.g. the TF Fzc1, the phosphodiesterase Pde2, and the kinases Ksp1, Arg2, and Iks1)

385   that negatively regulate capsule size (52, 80, 90).

386   Overall, we found that Pdr802 influences key cryptococcal phenotypes that

387   influence virulence, including quorum sensing, stress responses, Titan cell formation, and

388   capsule production (Figure 9). We have further identified multiple genes that are central

389   in these processes and are directly regulated by Pdr802. Some of these targets are also

390   regulated by calcineurin (e.g. Had1 and Crz1) or by another important TF, Gat201 (e.g.

391   Opt1, Liv3, Zfc3) (60, 75, 76). Finally, the expression of *PDR802* itself is regulated by the

392   TFs Gat201 and Hob1 (67, 76). The crosstalk between all of these regulatory

393   mechanisms remains to be dissected. Nonetheless, it is evident that Pdr802 is critical for

394   both survival in the lung and dissemination to the brain, thus explaining its role in

395   cryptococcal virulence.

396

MATERIALS AND METHODS

Strain construction and cell growth

399   We previously reported the *PDR802* deletion mutant (*pdr802*) in the KN99α strain

400   background (103) that was used in this work (39). Complementation of this mutant with

401   the wild-type gene at the native locus (*PDR802*) and construction of a strain that

402   expresses Pdr802 with N-terminal mCherry (mCherry-Pdr802) are detailed in the

403   Supplementary Methods. For all studies, *C. neoformans* strains were inoculated from

404   single colonies into YPD medium (2% [wt/vol] dextrose, 2% [wt/vol] Bacto peptone and

405   1% [wt/vol] yeast extract in double-distilled water [ddH$_2$O]) and grown overnight at 30°C

406   with shaking at 230 rpm before further handling as detailed below. To assess viability

407   during growth in tissue culture medium, overnight cultures were washed with phosphate-

408   buffered saline (PBS), diluted to 10^6 cells/ml in DMEM (Sigma, D6429), plated (1 ml/well)

409   in triplicate in 24-well plates, and incubated at 37°C and 5% CO_2. At the indicated times

410   cells were mixed thoroughly, diluted in PBS, and plated on YPD agar (YPD medium, 2%

411   agar [wt/vol]) for assessment of colony-forming units (CFU). To assess viability during

412   growth in mouse serum (prepared as below), YPD-grown cryptococcal cells (10^3) were

413   incubated in 100 μl of serum in 96-well plates for 24 h at 37°C and 5% CO_2 and CFU

414   assessed as above.

Animal experiments

416   All animal protocols were approved by the Washington University Institutional Animal

417   Care and Use Committee (reference 20170131) or Comissão de Ética no Uso de

418   Animais – CEUA (reference 30936), and care was taken to minimize handling and

419   discomfort. For survival studies, groups of five 4- to 6-week-old female C57BL/6 mice

420   (The Jackson Laboratory) were anesthetized by subcutaneous injection of 1.20 mg

421   ketamine and 0.24 mg xylazine in 120 μl sterile water and intranasally infected with 5 x

422   10^4 cryptococcal cells. The mice were monitored and humanely sacrificed when their

423   weight decreased to below 80% of initial weight or if they showed signs of disease, at

424   which point organ burden was assessed. The lungs and brains were harvested,

425   homogenized, diluted and plated on YPD agar. The resulting CFU were enumerated and

426   survival differences were assessed by Kaplan-Meier analysis.

427   For timed organ burden studies, *C. neoformans* overnight cultures were centrifuged

428   (1,000 x *g* for 3 min), washed with sterile PBS, and resuspended in PBS to 1 x 10^6

429   cells/ml. Groups of three 4- to 6-week-old female C57BL/6 mice (Centro Multidisciplinar

430   para Investigação Biológica na Área da Ciência em Animais de Laboratório, CEMIB)

431   were anesthetized as above and intranasally infected with 5 x 10^4 cryptococcal cells, and

432   monitored as above. At set time points post-infection (see text), mice were sacrificed and

433   fungal burden was assessed from organs (as above) or blood (obtained by cardiac

434   puncture). Organ burden was analyzed by Kruskal-Wallis test with Dunn's multiple

435   comparison *post hoc* test for each day post-infection.

436   To assess cryptococcal viability in mouse serum, 6 BALB/c mice were anesthetized with

437   isoflurane and blood was collected from the retro-orbital space using a sterile capillary

438   tube. Collected blood was incubated at 37°C for 30 min and serum was isolated by

439   centrifugation at 1,000 x *g* for 15 min and then heat-inactivated at 56 °C for 30 min.

440   **Capsule analysis**

441   To qualitatively assess capsule thickness, strains were grown in YPD medium for 16 h,

442   washed with PBS, and 10^6 cells were incubated in DMEM or mouse serum for 24 h at

443   37°C and 5% CO_2. After incubation, cells were fixed in 4% paraformaldehyde, washed

444   three times with PBS, and mixed with similar volumes of India ink for capsule

445   visualization and measurement as previously described (104).

446   For population-level capsule measurement, *C. neoformans* strains were grown overnight

447   in YPD, washed with PBS, and diluted to 10^6 cells/ml in DMEM. 150 µl aliquots were then

448   plated in quadruplicate in a poly-L-lysine coated 96-well plate (Fisher 655936) and

449   incubated at 37°C and 5% CO_2. After 24 hours, the cells were washed with PBS and

450   incubated with 150 µl of a staining mixture (100 µg/ml Calcofluor white to stain cell walls,

451   50 µg/ml of anticapsular monoclonal antibody 302 conjugated to Alexa Fluor 488

452   (Molecular probes), and 1.5% goat serum in PBS) for 30 minutes at room temperature in

453   the dark. The cells were washed again with PBS, fixed with 4% formaldehyde for 10

454   minutes at room temperature, washed with PBS, and each well refilled with 150 µl PBS.

21

455 The cells were imaged using a BioTek Cytation 3 imager, which automatically collected

456 100 images per well in a grid pattern at the well center. Image files were prepared for

457 analysis with the GE InCell Translator and assembled into .xdce image stacks for

458 analysis with the GE INCell Developer Toolbox 1.9. Cell wall and capsule images were

459 first filtered to remove background noise and border objects and then cells were identified

460 using shape-based object segmentation (3-pixel kernel, 50% sensitivity) followed by

461 watershed clump breaking to prevent apparent connectivity caused by incomplete

462 segmentation. Target linking was performed to assign each cell wall object to one

463 capsule object based on known 1:1 pairing and location, generating a target set. Capsule

464 and cell wall object diameters were calculated for each target set (hundreds to thousands

465 per well), and the difference between each pair of measurements was defined as the

466 capsule thickness. Data were normalized by the difference in capsule thickness between

467 uninduced and induced WT cells, which were included in each experiment, and

468 compared to hypercapsular (*pkr1*) (39) and hypocapsular (*ada2*) (105) control strains in

469 each experiment. Capsule sizes were compared by One-Way ANOVA with Dunnett's

470 multiple comparison *post hoc* test.

471 To measure capsule thickness of cryptococcal cells grown in the lungs of infected mice,

472 lung homogenates were filtered through a cell strainer with 40 μm pores using a syringe

473 plunger, fixed in 3.7% formaldehyde, and used for India ink staining and measurement as

474 above. For the visualization of KN99α and *PDR802* cells from mouse lungs after 18 days

475 of infection, the tissue was treated with 50 μg/ml DNAse I for 30 min at 37°C.

476 GXM immunoblotting was conducted as previously described (71). Briefly, 10^6 cells/ml

477 were grown in DMEM for 24 and 48h. Culture supernatant fractions were then resolved

22

478   by gel electrophoresis on 0.6% agarose, transferred onto nylon membranes, and probed

479   with 1 µg/ml anti-GXM antibody 302.

Phenotypic assays

481   For stress plates, cryptococcal cells were grown overnight in YPD, washed with PBS, and

482   diluted to 10^7 cells/ml in PBS. Aliquots (3 µl) of 10-fold serial dilutions were spotted on

483   YPD or YNB agar supplemented with various stressors (sorbitol, NaCl, $CaCl_2$, LiCl,

484   Congo Red, Calcofluor white, caffeine, SDS, $NaNO_2$, H_2O_2 and ethanol) in the

485   concentrations indicated in the figures. Melanization was tested on plates made by

486   mixing 10 ml of 2X minimal medium (2 g/L L-asparagine, 1 g/L $MgSO_4 \cdot 7H_2O$, 6 g/L

487   KH_2PO_4, 2 g/L thiamine, 2 mM L-3,4-dihydroxyphenylalanine [L-DOPA] and 0.1%

488   dextrose was added for melanization induction or 0.5% for melanization inhibition) with

489   10 ml of 2% agar-water per plate. A control strain lacking the ability to melanize was used

490   as a control (*lac1*) (88). For the solid urease assay, 10 µl of a 10^7 cells/ml suspension in

491   water was plated on Christensen's urea solid media (1 g/L peptone, 1 g/L dextrose, 5 g/L

492   NaCl, 0.8 g/L KH_2PO_4, 1.2 g/L Na_2HPO_4, 0.012 g/L phenol red and 15 g/L agar, pH 6.8).

493   Plates were incubated at 30°C or 37°C.

Titan cells

495   Titan cell induction was performed in 1x PBS supplemented with 10% heat inactivated

496   Fetal Calf Serum (FCS) for 72 hours at 37°C and 5% CO_2 as recently described (49) and

497   quantified by flow cytometry as previously reported (47, 48).

Phagocytosis

23

499   J774.16 cells were prepared for uptake experiments by seeding (10^5 cells/well) in a 96-

500   well plate and incubating in DMEM supplemented with 10% Fetal Bovine Serum (FBS) at

501   37°C and 5% CO_2 for 24 h. *C. neoformans* cells were prepared for uptake experiments

502   by inoculating an overnight culture in YPD into either DMEM or Titan cell induction

503   medium (49) and growing at 37°C and 5% CO_2 for 24 or 72 h, respectively. To initiate the

504   study, cryptococcal cells were washed with PBS and opsonized with anti-capsular

505   antibody 18B7 (1 µg/ml) for 1 h at 37°C while macrophages were activated with 50 nM

506   phorbol myristate acetate (PMA) for 1 h at 37°C and 5% CO_2; 10^6 cryptococcal cells were

507   then incubated with the macrophages for 2 h at 37°C and 5% CO_2. The wells were then

508   washed three times with warm PBS and the macrophages lysed with 0.1% Triton in PBS

509   and plated for CFU as above. Fold-change in CFU was assessed by comparison to the

510   CFU of opsonized cells. One-Way ANOVA with Dunnett's multiple comparison *post hoc*

511   test was used to compare phagocytosis of *pdr802* and *PDR802* strains with that of

512   KN99α.

Chromatin Immunoprecipitation (ChIP)

514   ChIP studies were performed as previously described (39, 105). Briefly, wild type and N-

515   terminal-mCherry-Pdr802 strains were cultivated in DMEM for 24 hours at 37°C and 5%

516   CO_2. The cells were then fixed with formaldehyde, lysed by mechanical bead-beating,

517   and the cell debris removed by centrifugation. The supernatant fraction was sheared by

518   sonication, centrifuged, and an aliquot was reserved as 'Input'. The remaining material

519   was incubated with rabbit IgG anti-mCherry antibody (Abcam, ab213511) tethered to

520   protein A sepharose ('IP') or sepharose alone ('Mock') overnight at 4°C. The beads were

521   then washed, incubated at 65°C to reverse DNA-DNA and DNA-protein crosslinks and

24

522 the DNA recovered by phenol/chloroform/isoamyl alcohol (25:24:1) extraction, ethanol

523 precipitation, and resuspension in nuclease-free water.

524 Samples were submitted to the Washington University Genome Technology Access

525 Center for library preparation and DNA samples were sequenced using the Illumina

526 Nextseq platform. The first replicate was sequenced using paired-end 2x75-bp reads and

527 replicates 2 and 3 were sequenced using single-end 75-bp reads; the minimum coverage

528 obtained was ~16x. The quality of the reads was evaluated by FastQC (106). Fastq files

529 were aligned to the KN99 genome (107) using NextGenMap 0.5.3 (108). SAM files were

530 converted to bam, reads were sorted and indexed, and read duplicates were removed

531 from the final bam files using samtools (109). Samtools was also used to filter out reads

532 with a mapping quality lesser than 20 phreds to guarantee single alignment of the reads.

533 Peaks were called using MACS2 (2.1.1.20160309) (110), filtered by size (maximum

534 threshold 5 kb and no minimum), and annotated using Homer 4.8 (111). The significant

535 peaks were chosen using the cutoff of fold enrichment above 2 and adjusted p value <

536 0.05 and read coverage of each peak was obtained using Samtools (109). Pdr802

537 binding motifs were identified using DREME (74); partial motifs were defined as at least 5

538 consecutive bp of the motif.

539 **RNA-Seq and Dual-Threshold Optimization (DTO)**

540 RNA from wild-type and *pdr802* cells grown for 24 hours in DMEM (37°C, 5% CO_2) was

541 isolated and sequenced as previously described (39). Briefly, cDNA samples were

542 sequenced using the Illumina Nextseq platform for single-end 1 x 75 bp reads and read

543 quality was evaluated by FastQC (106). Fastq files were aligned to the KN99 genome

544 (107) using Novoalign (112), SAM files were converted to bam, reads were sorted and

25

545   indexed, and read duplicates were removed from the final bam files using Samtools

546   (109). The number of reads mapped per gene was calculated using HTSeq (113) and

547   differential gene expression was analyzed with DESeq2 (114), using the Independent

548   Hypothesis Weighting (IHW) package to calculate the adjusted p-values (115). Dual-

549   Threshold Optimization (DTO) analysis was performed as recently described (77). This is

550   a method for simultaneously finding the best thresholds for significance in a TF binding

551   location dataset (e.g. ChIP) and a TF perturbation-response dataset (e.g. RNA-Seq of a

552   TF mutant). It works by trying out all pairs of thresholds for the two datasets, picking the

553   pair that minimizes the probability of the overlap between the bound and responsive gene

554   sets occurring by chance under a null model, and testing the significance of the overlap

555   by comparison to randomly permuted data. Our application of DTO to our ChIP and RNA-

556   Seq data yielded 1455 bound genes, 5186 responsive genes, and 1167 genes that were

557   both bound and responsive. Based on DTO, Pdr802 has an acceptable convergence

558   from binding and perturbation, with p value < 0.01 from the random permutation test and

559   minimum expected FDR less than or equal to 20% at 80% sensitivity. In addition to

560   requiring a statistically significant overlap between the ChIP-Seq and RNA-Seq gene

561   sets, we filtered out any genes for which traditional differential expression analysis

562   yielded an adjusted p-value ≤ 0.15 or absolute $\log_2$ of fold change ≥ 0.3, leaving 380

563   bound targets.

564   **Intracellular calcium measurement**

565   To measure intracellular free Ca^{2+}, yeast cells were cultured overnight in YPD at 30°C

566   with shaking, washed three times with deionized water, diluted to 10^6 cells/ml in DMEM

567   (Sigma, D6429), plated (1 ml/well) in triplicate in 24-well plates, and incubated at 37°C

568   and 5% CO_2 for 24 hours. At the indicated times, cells were mixed thoroughly, diluted in

569   PBS containing 2 µM Fluo4-AM (Thermo Fisher), incubated at 30°C for 30 min, and

570   analyzed using flow cytometry. The overnight culture was used as a control and treated

571   as above.

Data availability

573   ChIP-seq and RNA-seq data files are available at the NCBI Gene Expression Omnibus

574   under accession numbers GSE153134 and GSE162851, respectively.

575

REFERENCES

577   1.   Kwon-Chung KJ, Fraser JA, Doering TL, Wang ZA, Janbon G, Idnurm A, Bahn Y-

578   S. 2014. *Cryptococcus neoformans* and *Cryptococcus gattii*, the Etiologic Agents of

579   Cryptococcosis. Cold Spring Harb Perspect Med 4:a019760.

580   2.   Rajasingham R, Smith RM, Park BJ, Jarvis JN, Govender NP, Chiller TM, Denning

581   DW, Loyse A, Boulware DR. 2017. Global burden of disease of HIV-associated

582   cryptococcal meningitis: an updated analysis. Lancet Infect Dis 17:873–881.

583   3.   Ballou ER, Johnston SA. 2017. The cause and effect of *Cryptococcus* interactions

584   with the host. Curr Opin Microbiol 40:88–94.

585   4.   Sabiiti W, May RC. 2012. Mechanisms of infection by the human fungal pathogen

586   *Cryptococcus neoformans*. Future Microbiol 7:1297–1313.

587   5.   Garcia-Hermoso D, Janbon G, Dromer F. 1999. Epidemiological evidence for

588   dormant *Cryptococcus neoformans* infection. J Clin Microbiol 37:3204–3209.

6. Chang YC, Stins MF, McCaffery MJ, Miller GF, Pare DR, Dam T, Paul-Satyasee M, Kim KS, Kwon-Chung KJ. 2004. Cryptococcal yeast cells invade the central nervous system via transcellular penetration of the blood-brain barrier. Infect Immun 72:4985–4995.

7. Huang S-H, Long M, Wu C-H, Kwon-Chung KJ, Chang YC, Chi F, Lee S, Jong A. 2011. Invasion of *Cryptococcus neoformans* into Human Brain Microvascular Endothelial Cells Is Mediated through the Lipid Rafts-Endocytic Pathway via the Dual Specificity Tyrosine Phosphorylation-regulated Kinase 3 (DYRK3). J Biol Chem 286:34761–34769.

8. Jong A, Wu C-H, Shackleford GM, Kwon-Chung KJ, Chang YC, Chen H-M, Ouyang Y, Huang S-H. 2008. Involvement of human CD44 during *Cryptococcus neoformans* infection of brain microvascular endothelial cells. Cell Microbiol 10:1313–1326.

9. Maruvada R, Zhu L, Pearce D, Zheng Y, Perfect J, Kwon-Chung KJ, Kim KS. 2012. *Cryptococcus neoformans* phospholipase B1 activates host cell Rac1 for traversal across the blood-brain barrier. Cell Microbiol 14:1544–1553.

10. Chen SHM, Stins MF, Huang S-H, Chen YH, Kwon-Chung KJ, Chang Y, Kim KS, Suzuki K, Jong AY. 2003. *Cryptococcus neoformans* induces alterations in the cytoskeleton of human brain microvascular endothelial cells. J Med Microbiol 52:961–970.

11. Olszewski MA, Noverr MC, Chen G-H, Toews GB, Cox GM, Perfect JR, Huffnagle GB. 2004. Urease Expression by *Cryptococcus neoformans* Promotes Microvascular Sequestration, Thereby Enhancing Central Nervous System

612   Invasion. Am J Pathol 164:1761–1771.

613   12. Shi M, Li SS, Zheng C, Jones GJ, Kim KS, Zhou H, Kubes P, Mody CH. 2010.

614   Real-time imaging of trapping and urease-dependent transmigration of

615   *Cryptococcus neoformans* in mouse brain. J Clin Invest 120:1683–1693.

616   13. Santiago-Tirado FH, Onken MD, Cooper JA, Klein RS, Doering TL. 2017. Trojan

617   Horse Transit Contributes to Blood-Brain Barrier Crossing of a Eukaryotic

618   Pathogen. MBio 8:e02183-16.

619   14. Jarvis JN, Bicanic T, Loyse A, Namarika D, Jackson A, Nussbaum JC, Longley N,

620   Muzoora C, Phulusa J, Taseera K, Kanyembe C, Wilson D, Hosseinipour MC,

621   Brouwer AE, Limmathurotsakul D, White N, van der Horst C, Wood R, Meintjes G,

622   Bradley J, Jaffar S, Harrison T. 2014. Determinants of Mortality in a Combined

623   Cohort of 501 Patients With HIV-Associated Cryptococcal Meningitis: Implications

624   for Improving Outcomes. Clin Infect Dis 58:736–745.

625   15. John R. Perfect, William E. Dismukes, Francoise Dromer, David L. Goldman, John

626   R. Graybill, Richard J. Hamill, Thomas S. Harrison, Robert A. Larsen, Olivier

627   Lortholary, Minh-Hong Nguyen, Peter G. Pappas, William G. Powderly, Nina Singh,

628   Jack D. Sobel TCS. 2010. Clinical Practice Guidelines for the Management of

629   Cryptococcal Disease: 2010 Update by the Infectious Diseases Society of America.

630   Chinese J Infect Chemother 50:291–322.

631   16. Nosanchuk JD, Casadevall A. 2003. The contribution of melanin to microbial

632   pathogenesis. Cell Microbiol 5:203–223.

633   17. Singh A, Panting RJ, Varma A, Saijo T, Waldron KJ, Jong A, Ngamskulrungroj P,

634   Chang YC, Rutherford JC, Kwon-Chung KJ. 2013. Factors Required for Activation

635   of Urease as a Virulence Determinant in *Cryptococcus neoformans*. MBio

636   4:e00220-13.

637   18.   Chang YC, Kwon-Chung KJ. 1994. Complementation of a capsule-deficient

638   mutation of *Cryptococcus neoformans* restores its virulence. Mol Cell Biol 14:4912–

639   4919.

640   19.   Okagaki LH, Strain AK, Nielsen JN, Charlier C, Baltes NJ, Chrétien F, Heitman J,

641   Dromer F, Nielsen K. 2010. Cryptococcal Cell Morphology Affects Host Cell

642   Interactions and Pathogenicity. PLoS Pathog 6:e1000953.

643   20.   Zaragoza O, Nielsen K. 2013. Titan cells in *Cryptococcus neoformans*: cells with a

644   giant impact. Curr Opin Microbiol 16:409–413.

645   21.   Wang Y, Aisen P, Casadevall A. 1995. *Cryptococcus neoformans* melanin and

646   virulence: Mechanism of action. Infect Immun 63:3131–3136.

647   22.   Mednick AJ, Nosanchuk JD, Casadevall A. 2005. Melanization of *Cryptococcus*

648   *neoformans* Affects Lung Inflammatory Responses during Cryptococcal Infection.

649   Infect Immun 73:2012–2019.

650   23.   Wang Y, Casadevall A. 1994. Susceptibility of melanized and nonmelanized

651   *Cryptococcus neoformans* to nitrogen- and oxygen-derived oxidants. Infect Immun

652   62:3004–7.

653   24.   Doering TL, Nosanchuk JD, Roberts WK, Casadevall A. 1999. Melanin as a

654   potential cryptococcal defence against microbicidal proteins. Med Mycol 37:175–

655   81.

656   25.   Agustinho DP, Nosanchuk JD. 2017. Functions of Fungal MelaninsReference

657   Module in Life Sciences. Elsevier.

658   26.   Cox GM, Mukherjee J, Cole GT, Casadevall A, Perfect JR. 2000. Urease as a

659   virulence factor in experimental cryptococcosis. Infect Immun 68:443–8.

660   27.   Bose I, Reese AJ, Ory JJ, Janbon G, Doering TL. 2003. A Yeast under Cover: the

661   Capsule of *Cryptococcus neoformans*. Eukaryot Cell 2:655–663.

662   28.   Wang ZA, Li LX, Doering TL. 2018. Unraveling synthesis of the cryptococcal cell

663   wall and capsule. Glycobiology 28:719–730.

664   29.   Agustinho DP, Miller LC, Li LX, Doering TL. 2018. Peeling the onion: the outer

665   layers of *Cryptococcus neoformans*. Mem Inst Oswaldo Cruz 113:e180040.

666   30.   Bulmer GS, Sans MD. 1967. *Cryptococcus neoformans*. II. Phagocytosis by human

667   leukocytes. J Bacteriol 94:1480–3.

668   31.   Bulmer GS, Sans MD. 1968. *Cryptococcus neoformans*. 3. Inhibition of

669   phagocytosis. 95:5–8.

670   32.   Tacker JR, Farhi F, Bulmer GS. 1972. Intracellular fate of *Cryptococcus*

671   *neoformans*. Infect Immun 6:162–7.

672   33.   Monari C, Bistoni F, Vecchiarelli A. 2006. Glucuronoxylomannan exhibits potent

673   immunosuppressive properties. FEMS Yeast Res 6:537–542.

674   34.   Hayes JB, Sircy LM, Heusinkveld LE, Ding W, Leander RN, McClelland EE, Nelson

675   DE. 2016. Modulation of Macrophage Inflammatory Nuclear Factor κB (NF-κB)

676   Signaling by Intracellular *Cryptococcus neoformans*. J Biol Chem 291:15614–

677   15627.

678   35.   Fonseca FL, Nohara LL, Cordero RJB, Frases S, Casadevall A, Almeida IC,

679   Nimrichter L, Rodrigues ML. 2010. Immunomodulatory Effects of Serotype B

680   Glucuronoxylomannan from *Cryptococcus gattii* Correlate with Polysaccharide

681   Diameter. Infect Immun 78:3861–3870.

682   36.   Garcia-Hermoso D, Dromer F, Janbon G. 2004. *Cryptococcus neoformans* Capsule

683   Structure Evolution *In Vitro* and during Murine Infection. Infect Immun 72:3359–

684   3365.

685   37.   Guimarães AJ, Frases S, Cordero RJB, Nimrichter L, Casadevall A, Nosanchuk

686   JD. 2010. *Cryptococcus neoformans* responds to mannitol by increasing capsule

687   size *in vitro* and *in vivo*. Cell Microbiol 12:740–753.

688   38.   Cordero RJB, Pontes B, Guimarães AJ, Martinez LR, Rivera J, Fries BC,

689   Nimrichter L, Rodrigues ML, Viana NB, Casadevall A. 2011. Chronological Aging Is

690   Associated with Biophysical and Chemical Changes in the Capsule of

691   *Cryptococcus neoformans*. Infect Immun 79:4990–5000.

692   39.   Maier EJ, Haynes BC, Gish SR, Wang ZA, Skowyra ML, Marulli AL, Doering TL,

693   Brent MR. 2015. Model-driven mapping of transcriptional networks reveals the

694   circuitry and dynamics of virulence regulation. Genome Res 25:690–700.

695   40.   Santos JRA, Holanda RA, Frases S, Bravim M, Araujo GDS, Santos PC, Costa

696   MC, Ribeiro MJA, Ferreira GF, Baltazar LM, Miranda AS, Oliveira DB, Santos

697   CMA, Fontes ACL, Gouveia LF, Resende-Stoianoff MA, Abrahão JS, Teixeira AL,

698   Paixão TA, Souza DG, Santos DA. 2014. Fluconazole Alters the Polysaccharide

699   Capsule of *Cryptococcus gattii* and Leads to Distinct Behaviors in Murine

700   Cryptococcosis. PLoS One 9:e112669.

701   41.   Silveira CP, Piffer AC, Kmetzsch L, Fonseca FL, Soares DA, Staats CC, Rodrigues

702   ML, Schrank A, Vainstein MH. 2013. The heat shock protein (Hsp) 70 of

703   *Cryptococcus neoformans* is associated with the fungal cell surface and influences

704   the interaction between yeast and host cells. Fungal Genet Biol 60:53–63.

705   42.   Alspaugh JA. 2015. Virulence mechanisms and *Cryptococcus neoformans*

706   pathogenesis. Fungal Genet Biol 78:55–58.

707   43.   García-Rodas R, de Oliveira H, Trevijano-Contador N, Zaragoza O. 2018.

708   Cryptococcal Titan Cells: When Yeast Cells Are All Grown up, p. 101–120. *In*

709   Current Topics in Microbiology and Immunology. Springer Verlag.

710   44.   Zhou X, Ballou ER. 2018. The *Cryptococcus neoformans* Titan Cell: From *In Vivo*

711   Phenomenon to *In Vitro* Model. Curr Clin Microbiol Reports 5:252–260.

712   45.   Zaragoza O, García-Rodas R, Nosanchuk JD, Cuenca-Estrella M, Rodríguez-

713   Tudela JL, Casadevall A. 2010. Fungal Cell Gigantism during Mammalian Infection.

714   PLoS Pathog 6:e1000945.

715   46.   Gerstein AC, Fu MS, Mukaremera L, Li Z, Ormerod KL, Fraser JA, Berman J,

716   Nielsen K. 2015. Polyploid Titan Cells Produce Haploid and Aneuploid Progeny To

717   Promote Stress Adaptation. MBio 6:e01340-15.

718   47.   Hommel B, Mukaremera L, Cordero RJB, Coelho C, Desjardins CA, Sturny-Leclère

719   A, Janbon G, Perfect JR, Fraser JA, Casadevall A, Cuomo CA, Dromer F, Nielsen

720   K, Alanio A. 2018. Titan cells formation in *Cryptococcus neoformans* is finely tuned

721   by environmental conditions and modulated by positive and negative genetic

722   regulators. PLOS Pathog 14:e1006982.

723 48. Trevijano-Contador N, de Oliveira HC, García-Rodas R, Rossi SA, Llorente I,

724   Zaballos Á, Janbon G, Ariño J, Zaragoza Ó. 2018. *Cryptococcus neoformans* can

725   form titan-like cells *in vitro* in response to multiple signals. PLOS Pathog

726   14:e1007007.

727 49. Dambuza IM, Drake T, Chapuis A, Zhou X, Correia J, Taylor-Smith L, LeGrave N,

728   Rasmussen T, Fisher MC, Bicanic T, Harrison TS, Jaspars M, May RC, Brown GD,

729   Yuecel R, MacCallum DM, Ballou ER. 2018. The *Cryptococcus neoformans* Titan

730   cell is an inducible and regulated morphotype underlying pathogenesis. PLOS

731   Pathog 14:e1006978.

732 50. García-Barbazán I, Trevijano-Contador N, Rueda C, de Andrés B, Pérez-Tavárez

733   R, Herrero-Fernández I, Gaspar ML, Zaragoza O. 2016. The formation of titan cells

734   in *Cryptococcus neoformans* depends on the mouse strain and correlates with

735   induction of Th2-type responses. Cell Microbiol 18:111–124.

736 51. Mukaremera L, Lee KK, Wagener J, Wiesner DL, Gow NAR, Nielsen K. 2018. Titan

737   cell production in *Cryptococcus neoformans* reshapes the cell wall and capsule

738   composition during infection. Cell Surf 1:15–24.

739 52. Jung K-W, Yang D-H, Maeng S, Lee K-T, So Y-S, Hong J, Choi J, Byun H-J, Kim

740   H, Bang S, Song M-H, Lee J-W, Kim MS, Kim S-Y, Ji J-H, Park G, Kwon H, Cha S,

741   Meyers GL, Wang LL, Jang J, Janbon G, Adedoyin G, Kim T, Averette AK,

742   Heitman J, Cheong E, Lee Y-H, Lee Y-W, Bahn Y-S. 2015. Systematic functional

743   profiling of transcription factor networks in *Cryptococcus neoformans*. Nat Commun

744   6:6757.

745   53.   Schneider R de O, Fogaça N de SS, Kmetzsch L, Schrank A, Vainstein MH, Staats

746   CC. 2012. Zap1 Regulates Zinc Homeostasis and Modulates Virulence in

747   *Cryptococcus gattii*. PLoS One 7:e43773.

748   54.   Garcia-Santamarina S, Festa RA, Smith AD, Yu C-H, Probst C, Ding C, Homer

749   CM, Yin J, Noonan JP, Madhani H, Perfect JR, Thiele DJ. 2018. Genome-wide

750   analysis of the regulation of Cu metabolism in *Cryptococcus neoformans*. Mol

751   Microbiol 108:473–494.

752   55.   Lev S, Kaufman-Francis K, Desmarini D, Juillard PG, Li C, Stifter SA, Feng CG,

753   Sorrell TC, Grau GER, Bahn Y-S, Djordjevic JT. 2017. Pho4 Is Essential for

754   Dissemination of *Cryptococcus neoformans* to the Host Brain by Promoting

755   Phosphate Uptake and Growth at Alkaline pH. mSphere 2:e00381-16.

756   56.   Jung WH, Sham A, White R, Kronstad JW. 2006. Iron Regulation of the Major

757   Virulence Factors in the AIDS-Associated Pathogen *Cryptococcus neoformans*.

758   PLoS Biol 4:e410.

759   57.   Chow EWL, Clancey SA, Billmyre RB, Averette AF, Granek JA, Mieczkowski P,

760   Cardenas ME, Heitman J. 2017. Elucidation of the calcineurin-Crz1 stress

761   response transcriptional network in the human fungal pathogen *Cryptococcus

762   neoformans*. PLOS Genet 13:e1006667.

763   58.   O'Meara TR, Norton D, Price MS, Hay C, Clements MF, Nichols CB, Alspaugh JA.

764   2010. Interaction of *Cryptococcus neoformans* Rim101 and Protein Kinase A

765   Regulates Capsule. PLoS Pathog 6:e1000776.

766   59.   Gish SR, Maier EJ, Haynes BC, Santiago-Tirado FH, Srikanta DL, Ma CZ, Li LX,

767   Williams M, Crouch EC, Khader SA, Brent MR, Doering TL. 2016. Computational

768   Analysis Reveals a Key Regulator of Cryptococcal Virulence and Determinant of

769   Host Response. MBio 7:e00313-16.

770   60.   Chun CD, Brown JCS, Madhani HD. 2011. A Major Role for Capsule-Independent

771   Phagocytosis-Inhibitory Mechanisms in Mammalian Infection by *Cryptococcus*

772   *neoformans*. Cell Host Microbe 9:243–251.

773   61.   Moranova Z, Virtudazo E, Hricova K, Ohkusu M, Kawamoto S, Husickova V,

774   Raclavsky V. 2014. The CRZ1/SP1-like gene links survival under limited aeration,

775   cell integrity and biofilm formation in the pathogenic yeast *Cryptococcus*

776   *neoformans*. Biomed Pap 158:212–220.

777   62.   Lev S, Desmarini D, Chayakulkeeree M, Sorrell TC, Djordjevic JT. 2012. The

778   Crz1/Sp1 Transcription Factor of *Cryptococcus neoformans* Is Activated by

779   Calcineurin and Regulates Cell Wall Integrity. PLoS One 7:e51403.

780   63.   Park H-S, Chow EWL, Fu C, Soderblom EJ, Moseley MA, Heitman J, Cardenas

781   ME. 2016. Calcineurin Targets Involved in Stress Survival and Fungal Virulence.

782   PLOS Pathog 12:e1005873.

783   64.   Lee D, Jang E-H, Lee M, Kim S-W, Lee Y, Lee K-T, Bahn Y-S. 2019. Unraveling

784   Melanin Biosynthesis and Signaling Networks in *Cryptococcus neoformans*. MBio

785   10:e02267-19.

786   65.   Rhodes J, Desjardins CA, Sykes SM, Beale MA, Vanhove M, Sakthikumar S, Chen

787   Y, Gujja S, Saif S, Chowdhary A, Lawson DJ, Ponzio V, Colombo AL, Meyer W,

788   Engelthaler DM, Hagen F, Illnait-Zaragozi MT, Alanio A, Vreulink J-M, Heitman J,

789   Perfect JR, Litvintseva AP, Bicanic T, Harrison TS, Fisher MC, Cuomo CA. 2017.

790   Tracing Genetic Exchange and Biogeography of *Cryptococcus neoformans* var.

791   *grubii* at the Global Population Level. Genetics 207:327–346.

792 66. Liu OW, Chun CD, Chow ED, Chen C, Madhani HD, Noble SM. 2008. Systematic

793   Genetic Analysis of Virulence in the Human Fungal Pathogen *Cryptococcus*

794   *neoformans*. Cell 135:174–188.

795 67. Lee K-T, Hong J, Lee D-G, Lee M, Cha S, Lim Y-G, Jung K-W, Hwangbo A, Lee Y,

796   Yu S-J, Chen Y-L, Lee J-S, Cheong E, Bahn Y-S. 2020. Fungal kinases and

797   transcription factors regulating brain infection in *Cryptococcus neoformans*. Nat

798   Commun 11:1521.

799 68. Krysan DJ, Zhai B, Beattie SR, Misel KM, Wellington M, Lin X. 2019. Host Carbon

800   Dioxide Concentration Is an Independent Stress for *Cryptococcus neoformans* That

801   Affects Virulence and Antifungal Susceptibility. MBio 10:e01410-19.

802 69. D'Souza CA, Alspaugh JA, Yue C, Harashima T, Cox GM, Perfect JR, Heitman J.

803   2001. Cyclic AMP-Dependent Protein Kinase Controls Virulence of the Fungal

804   Pathogen *Cryptococcus neoformans*. Mol Cell Biol 21:3179–3191.

805 70. Hu G, Steen BR, Lian T, Sham AP, Tam N, Tangen KL, Kronstad JW. 2007.

806   Transcriptional Regulation by Protein Kinase A in *Cryptococcus neoformans*. PLoS

807   Pathog 3:e42.

808 71. Yoneda A, Doering TL. 2008. Regulation of *Cryptococcus neoformans* Capsule

809   Size Is Mediated at the Polymer Level. Eukaryot Cell 7:546–549.

810   72.   Frases S, Pontes B, Nimrichter L, Viana NB, Rodrigues ML, Casadevall A. 2009.

811   Capsule of *Cryptococcus neoformans* grows by enlargement of polysaccharide

812   molecules. Proc Natl Acad Sci U S A 106:1228–1233.

813   73.   Gaylord EA, Choy HL, Doering TL. 2020. Dangerous Liaisons: Interactions of

814   *Cryptococcus neoformans* with Host Phagocytes. Pathogens 9:891.

815   74.   Bailey TL. 2011. DREME: Supp. Bioinformatics 27:1653–1659.

816   75.   Summers DK, Perry DS, Rao B, Madhani HD. 2020. Coordinate genomic

817   association of transcription factors controlled by an imported quorum sensing

818   peptide in *Cryptococcus neoformans*. PLOS Genet 16:e1008744.

819   76.   Homer CM, Summers DK, Goranov AI, Clarke SC, Wiesner DL, Diedrich JK,

820   Moresco JJ, Toffaletti D, Upadhya R, Caradonna I, Petnic S, Pessino V, Cuomo

821   CA, Lodge JK, Perfect J, Yates 3rd JR, Nielsen K, Craik CS, Madhani HD. 2016.

822   Intracellular Action of a Secreted Peptide Required for Fungal Virulence. Cell Host

823   Microbe 19:849–864.

824   77.   Kang Y, Patel NR, Shively C, Recio PS, Chen X, Wranik BJ, Kim G, Scott McIsaac

825   R, Mitra R, Brent MR. 2020. Dual threshold optimization and network inference

826   reveal convergent evidence from TF binding locations and TF perturbation

827   responses. Genome Res 30:459–471.

828   78.   Giles SS, Stajich JE, Nichols C, Gerrald QD, Alspaugh JA, Dietrich F, Perfect JR.

829   2006. The *Cryptococcus neoformans* catalase gene family and its role in

830   antioxidant defense. Eukaryot Cell 5:1447–1459.

831   79.   Cox GM, Harrison TS, McDade HC, Taborda CP, Heinrich G, Casadevall A,

832   Perfect JR. 2003. Superoxide dismutase influences the virulence of *Cryptococcus*

833   *neoformans* by affecting growth within macrophages. Infect Immun 71:173–80.

834   80.   Lee K-T, So Y-S, Yang D-H, Jung K-W, Choi J, Lee D-G, Kwon H, Jang J, Wang

835   LL, Cha S, Meyers GL, Jeong E, Jin J-H, Lee Y, Hong J, Bang S, Ji J-H, Park G,

836   Byun H-J, Park SW, Park Y-M, Adedoyin G, Kim T, Averette AF, Choi J-S, Heitman

837   J, Cheong E, Lee Y-H, Bahn Y-S. 2016. Systematic functional analysis of kinases

838   in the fungal pathogen *Cryptococcus neoformans*. Nat Commun 7:12766.

839   81.   Caza M, Hu G, Price M, Perfect JR, Kronstad JW. 2016. The Zinc Finger Protein

840   Mig1 Regulates Mitochondrial Function and Azole Drug Susceptibility in the

841   Pathogenic Fungus *Cryptococcus neoformans*. mSphere 1.

842   82.   Chen Y, Toffaletti DL, Tenor JL, Litvintseva AP, Fang C, Mitchell TG, McDonald

843   TR, Nielsen K, Boulware DR, Bicanic T, Perfect JR. 2014. The *Cryptococcus*

844   *neoformans* transcriptome at the site of human meningitis. MBio 5:e01087-13.

845   83.   Alspaugh JA, Pukkila-Worley R, Harashima T, Cavallo LM, Funnell D, Cox GM,

846   Perfect JR, Kronstad JW, Heitman J. 2002. Adenylyl cyclase functions downstream

847   of the Gα protein Gpa1 and controls mating and pathogenicity of *Cryptococcus*

848   *neoformans*. Eukaryot Cell 1:75–84.

849   84.   Heung LJ, Kaiser AE, Luberto C, Del Poeta M. 2005. The role and mechanism of

850   diacylglycerol-protein kinase C1 signaling in melanogenesis by *Cryptococcus*

851   *neoformans*. J Biol Chem 280:28547–28555.

852   85.   Gerik KJ, Bhimireddy SR, Ryerse JS, Specht CA, Lodge JK. 2008. PKC1 is

853   essential for protection against both oxidative and nitrosative stresses, cell integrity,

854   and normal manifestation of virulence factors in the pathogenic fungus

855   *Cryptococcus neoformans*. Eukaryot Cell 7:1685–1698.

856   86.   Waterman SR, Hacham M, Hu G, Zhu X, Park Y-D, Shin S, Panepinto J, Valyi-

857   Nagy T, Beam C, Husain S, Singh N, Williamson PR. 2007. Role of a CUF1/CTR4

858   copper regulatory axis in the virulence of *Cryptococcus neoformans*. J Clin Invest

859   117:794–802.

860   87.   Jiang N, Sun N, Xiao D, Pan J, Wang Y, Zhu X. 2009. A copper-responsive factor

861   gene *CUF1* required for copper induction of laccase in *Cryptococcus neoformans*.

862   FEMS Microbiol Lett 296:84–90.

863   88.   Walton FJ, Idnurm A, Heitman J. 2005. Novel gene functions required for

864   melanization of the human pathogen *Cryptococcus neoformans*. Mol Microbiol

865   57:1381–1396.

866   89.   Cheon SA, Jung K-W, Chen Y-L, Heitman J, Bahn Y-S, Kang HA. 2011. Unique

867   Evolution of the UPR Pathway with a Novel bZIP Transcription Factor, Hxl1, for

868   Controlling Pathogenicity of *Cryptococcus neoformans*. PLoS Pathog 7:e1002177.

869   90.   Hicks JK, Bahn YS, Heitman J. 2005. Pde1 phosphodiesterase modulates cyclic

870   AMP levels through a protein kinase A-mediated negative feedback loop in

871   *Cryptococcus neoformans*. Eukaryot Cell 4:1971–1981.

872   91.   Kozubowski L, Lee SC, Heitman J. 2009. Signalling pathways in the pathogenesis

873   of *Cryptococcus*. Cell Microbiol 11:370–380.

874   92.   Fox DS, Cruz MC, Sia RAL, Ke H, Cox GM, Cardenas ME, Heitman J. 2001.

875   Calcineurin regulatory subunit is essential for virulence and mediates interactions

876   with FKBP12-FK506 in *Cryptococcus neoformans*. Mol Microbiol 39:835–849.

877   93. Odom A. 1997. Calcineurin is required for virulence of *Cryptococcus neoformans*.

878   EMBO J 16:2576–2589.

879   94. Jung W-H, Son Y-E, Oh S-H, Fu C, Kim HS, Kwak J-H, Cardenas ME, Heitman J,

880   Park H-S. 2018. Had1 Is Required for Cell Wall Integrity and Fungal Virulence in

881   *Cryptococcus neoformans*. Genes|Genomes|Genetics 8:643–652.

882   95. Kmetzsch L, Staats CC, Cupertino JB, Fonseca FL, Rodrigues ML, Schrank A,

883   Vainstein MH. 2013. The calcium transporter Pmc1 provides Ca2+ tolerance and

884   influences the progression of murine cryptococcal infection. FEBS J 280:4853–

885   4864.

886   96. Kmetzsch L, Staats CC, Simon E, Fonseca FL, de Oliveira DL, Sobrino L,

887   Rodrigues J, Leal AL, Nimrichter L, Rodrigues ML, Schrank A, Vainstein MH. 2010.

888   The Vacuolar Ca2+ Exchanger Vcx1 Is Involved In Calcineurin-Dependent Ca2+

889   Tolerance and Virulence in *Cryptococcus neoformans*. Eukaryot Cell 9:1798–1805.

890   97. Denham S, Brown J. 2018. Mechanisms of Pulmonary Escape and Dissemination

891   by *Cryptococcus neoformans*. J Fungi 4:25.

892   98. Sun D, Sun P, Li H, Zhang M, Liu G, Strickland AB, Chen Y, Fu Y, Xu J, Yosri M,

893   Nan Y, Zhou H, Zhang X, Shi M. 2019. Fungal dissemination is limited by liver

894   macrophage filtration of the blood. Nat Commun 10:4566.

895   99. Santiago-Tirado FH, Doering TL. 2017. False friends: Phagocytes as Trojan horses

896   in microbial brain infections. PLOS Pathog 13:e1006680.

897   100. Squizani ED, Oliveira NK, Reuwsaat JCV, Marques BM, Lopes W, Gerber AL, de

898   Vasconcelos ATR, Lev S, Djordjevic JT, Schrank A, Vainstein MH, Staats CC,

899   Kmetzsch L. 2018. Cryptococcal dissemination to the central nervous system

900   requires the vacuolar calcium transporter Pmc1. Cell Microbiol 20:e12803.

901   101. Okagaki LH, Nielsen K. 2012. Titan Cells Confer Protection from Phagocytosis in

902   *Cryptococcus neoformans* Infections. Eukaryot Cell 11:820–826.

903   102. Srikanta D, Santiago-Tirado FH, Doering TL. 2014. *Cryptococcus neoformans*:

904   historical curiosity to modern pathogen. Yeast 31:47–60.

905   103. Nielsen K, Cox GM, Wang P, Toffaletti DL, Perfect JR, Heitman J. 2003. Sexual

906   Cycle of *Cryptococcus neoformans* var. *grubii* and Virulence of Congenic a and α

907   Isolates. Infect Immun 71:4831–4841.

908   104. Reuwsaat JCV, Motta H, Garcia AWA, Vasconcelos CB, Marques BM, Oliveira NK,

909   Rodrigues J, Ferrareze PAG, Frases S, Lopes W, Barcellos VA, Squizani ED,

910   Horta JA, Schrank A, Rodrigues ML, Staats CC, Vainstein MH, Kmetzsch L. 2018.

911   A Predicted Mannoprotein Participates in *Cryptococcus gattii* Capsular Structure.

912   mSphere 3:e00023-18.

913   105. Haynes BC, Skowyra ML, Spencer SJ, Gish SR, Williams M, Held EP, Brent MR,

914   Doering TL. 2011. Toward an Integrated Model of Capsule Regulation in

915   *Cryptococcus neoformans*. PLoS Pathog 7:e1002411.

916   106.   Babraham Bioinformatics - FastQC A Quality Control tool for High Throughput

917   Sequence Data.

918   107. Friedman RZ, Gish SR, Brown H, Brier L, Howard N, Doering TL, Brent MR. 2018.

919   Unintended Side Effects of Transformation Are Very Rare in *Cryptococcus*

920   *neoformans*. Genes|Genomes|Genetics 8:815–822.

921   108. Sedlazeck FJ, Rescheneder P, von Haeseler A. 2013. NextGenMap: fast and

922   accurate read mapping in highly polymorphic genomes. Bioinformatics 29:2790–1.

923   109. Li H, Handsaker B, Wysoker A, Fennell T, Ruan J, Homer N, Marth G, Abecasis G,

924   Durbin R, 1000 Genome Project Data Processing Subgroup. 2009. The Sequence

925   Alignment/Map format and SAMtools. Bioinformatics 25:2078–2079.

926   110. Zhang Y, Liu T, Meyer CA, Eeckhoute J, Johnson DS, Bernstein BE, Nussbaum C,

927   Myers RM, Brown M, Li W, Liu XS. 2008. Model-based Analysis of ChIP-Seq

928   (MACS). Genome Biol 9:R137.

929   111. Heinz S, Benner C, Spann N, Bertolino E, Lin YC, Laslo P, Cheng JX, Murre C,

930   Singh H, Glass CK. 2010. Simple combinations of lineage-determining transcription

931   factors prime cis-regulatory elements required for macrophage and B cell identities.

932   Mol Cell 38:576–89.

933   112.   Novocraft. www.novocraft.com.

934   113. Anders S, Pyl PT, Huber W. 2015. HTSeq--a Python framework to work with high-

935   throughput sequencing data. Bioinformatics 31:166–169.

936   114. Love MI, Huber W, Anders S. 2014. Moderated estimation of fold change and

937   dispersion for RNA-seq data with DESeq2. Genome Biol 15:550.

938   115. Ignatiadis N, Klaus B, Zaugg JB, Huber W. 2016. Data-driven hypothesis weighting

939   increases detection power in genome-scale multiple testing. Nat Methods 13:577–

940   580.

116. Li LX, Rautengarten C, Heazlewood JL, Doering TL. 2018. Xylose donor transport is critical for fungal virulence. PLOS Pathog 14:e1006765.

ACKNOWLEDGMENTS

AUTHORS CONTRIBUTION

963

964 Conceived and designed experiments: J.C.V.R., D.P.A., A.L.C., M.R.B., L.K. and T.L.D.;

965 Performed experiments: J.C.V.R., D.P.A., H.M., H.B., and A.L.C;

966 Analyzed data: J.C.V.R., D.P.A., A.L.C., M.R.B., L.K. and T.L.D.;

967 Contributed reagents and materials: M.R.B., L.K. and T.L.D.;

968 Drafted the paper: J.C.V.R, L.K. and T.L.D.

969 Revised the paper: J.C.V.R., D.P.A., M.R.B., L.K. and T.L.D.

970

971 **COMPETING INTERESTS**

972 The authors declare no competing financial interests.

973

974 **TABLES**

975 **Table 1. Pdr802 targets involved in quorum sensing and Titan cell formation.**

976

977 **Table 2. Genes regulated by Pdr802 involved in adaptation to the host**

978 **environment.**

979

980 **FIGURE LEGENDS**

981 **Figure 1. The transcription factor Pdr802 influences *C. neoformans* virulence.** A.

982 Survival of C57BL/6 mice over time after intranasal inoculation with 5×10^4 cryptococci of

983 the strains indicated, with sacrifice triggered by weight below 80% of peak. B. Mean +/-

984 SD of total colony-forming units (CFU) in lung tissue at various times post-infection. CFU

985 inoculated for each strain were 41,400 (KN99α), 42,800 (*pdr802*) and 26,600 (*PDR802*).

986 p<0.05 for *pdr802* compared to the other strains at all time points.

987

988 **Figure 2. *PDR802* expression is required for cell viability and induced during**

989 **growth in host-like conditions.** A. Cells grown in DMEM at 37°C and 5% CO_2 were

990 sampled at the times indicated and plated on YPD to assess viability (measured by CFU

991 and plotted as fold-change from time 0). B. *PDR802* expression in KN99α cells grown in

992 DMEM at 37°C and 5% CO_2 was assessed by RNA-seq as in Li *et al*., 2018 (116).

993

994 **Figure 3. The *pdr802* mutant is hypercapsular.** A. Representative

995 immunofluorescence micrographs of the indicated strains after growth in DMEM (37°C,

996 5% CO_2) for 24 hours. The capsule was stained with monoclonal antibody anti-GXM 302

997 conjugated with Alexa 488 (green) and the cell wall with Calcofluor White (blue). All

998 images are to the same scale; scale bar, 5 μm. B. Capsule thickness distribution for the

999 indicated strains. C. Mean +/- SD of capsule size, quantified as detailed in the Methods

1000 and Figure S5, with *pkr1* (39) and *ada2* (105) shown as hypercapsular and hypocapsular

1001 controls, respectively. ****, p<0.0001 compared to KN99α by one-way ANOVA with

1002 posthoc Dunnett test.

1003

46

1004 **Figure 4. Growth in mouse serum elicits increased capsule thickness and cell body**

1005 **diameter in the *pdr802* mutant.** A. Light micrographs of the indicated strains after

1006 growth in mouse serum (at 37°C, 5% CO_2) for 24 h and negative staining with India ink to

1007 visualize the capsule. All images are to the same scale; scale bar, 5 μm. B. Mean +/- SD

1008 of capsule thickness, assessed by measuring at least 50 cells per strain with ImageJ. C.

1009 Cells grown as in Panel A were plated on YPD to assess CFU. Mean +/- SD of the fold-

1010 change compared to 0 h is shown. D. Mean +/- SD of cell body diameter, measured as in

1011 B. ***, $p<0.001$ and ****, $p<0.0001$ for comparison of *pdr802* results to KN99α by one-

1012 way ANOVA with posthoc Dunnett test.

1013

1014 **Figure 5. Absence of *PDR802* yields enlarged cells and loss of capsule induction in**

1015 **the context of animal infection.** A. India ink staining of fungi isolated from the lungs of

1016 mice infected with the indicated strains. Numbers at left indicate the days post-infection.

1017 All images are to the same scale; scale bar, 10 μm. B and C. Mean +/- SD of cell body

1018 diameter (B) and capsule thickness (C), assessed by measuring at least 50 cells per

1019 strain with ImageJ. ****, $p<0.0001$ and ***, $p<0.001$ for comparison of *pdr802* results to

1020 KN99α or *PDR802* by one-way ANOVA with posthoc Dunnett test for each day post-

1021 infection.

1022

1023 **Figure 6. Pdr802 is a negative regulator of Titan cell formation.** Left, cultures were

1024 subjected to *in vitro* conditions that induce Titan cell formation and imaged with India Ink.

1025 All images are to the same scale; scale bar, 10 μm. Images were selected so that each

1026 shows multiple examples of Titan cells, not to reflect abundance of this morphotype.

1027   Right, the percent of Titan cells (TC) in each culture was quantified using flow cytometry,

1028   gated as indicated by the blue square. FSC, forward scatter; SSC, side scatter.

1029

1030   **Figure 7. Deletion of *PDR802* affects phagocytosis after growth under conditions**

1031   **that induce capsule and Titan cell formation.** The indicated *C. neoformans* strains

1032   were grown in YPD (18 h), DMEM (24 h), or Titan-cell induction medium (72 h) and then

1033   incubated for 2 h with J774.16 mouse macrophages; host cells were then washed and

1034   lysed to assess fungal burden by CFU. Data shown are normalized to the CFU of the

1035   initial inoculum. *, $p < 0.05$ and **, $p < 0.01$ compared to KN99α by one-way ANOVA with

1036   posthoc Dunnett test.

1037

1038   **Figure 8. Pdr802 participates in calcineurin signaling.** *Panels A-B*. Interactions of

1039   Pdr802 with upstream regions of the indicated genes. The ratios ($\log_2$) of reads from

1040   immunoprecipitated (IP) DNA to input DNA were calculated for 1,000 bp upstream of the

1041   first coding nucleotide (+1); shown is the difference in these values between tagged and

1042   untagged strains. Black triangles, complete Pdr802 DNA-binding motifs (Figure S7B);

1043   gray triangles, partial motifs. C. Intracellular calcium measurement by flow cytometry

1044   using Fluo-4AM. Each column shows the mean and standard deviation of three biological

1045   replicates. ***, $p < 0.001$ and ****, $p < 0.0001$ by one-way ANOVA with posthoc Dunnett

1046   test.

1047

1048 **Figure 9. Pdr802 mode of action.** *Left panel*. When wild-type *C. neoformans* enters a

1049 host, *PDR802* expression is induced and Pdr802 positively regulates elements of the

1050 quorum sensing pathway (described in the text) as well as expression of TFs implicated

1051 in this pathway (*LIV3*), brain infectivity (*STB4*), and Titan cell production (*ZFC3*). At the

1052 same time, Pdr802 regulates two calcineurin targets (*CRZ1* and *HAD1*) and a variety of

1053 other genes (see text). Shown are examples of genes involved in the response to

1054 oxidative stress (*SOD1*), growth at 37°C (*KIC1*), urease activity (*GUT1*), capsule

1055 production (*BZP4*), and cell wall remodeling (*MP98*). *Right panel*. In the absence of these

1056 regulatory changes, *pdr802* cells are poorly equipped to survive the stress of the host

1057 environment and are subject to increased intracellular calcium levels, dysregulation of

1058 capsule production, and impaired stress resistance. As a result, the cryptococcal

1059 population in the lung is smaller and is enriched in Titan cells and hypercapsular cells of

1060 normal size, both of which demonstrate reduced phagocytosis by host cells and impaired

1061 ability to cross biological barriers; these defects reduce dissemination to the central

1062 nervous system.

1063

1064 **SUPPLEMENTAL FIGURE LEGENDS**

1065 **Figure S1. Mutant strain construction and confirmation.** A. Scheme for generating *C.*

1066 *neoformans* strains in the KN99α background (middle) that either lack *PDR802* (*pdr802,*

1067 top) or encode a tagged copy of the protein (*mCherry-PDR802*). B. Qualitative analysis of

1068 gene expression in Panel A strains and the complemented *pdr802* mutant (*PDR802*).

1069 Cryptococcal mRNA isolated from cells grown in DMEM (37°C, 5% CO_2, 24 hours) was

1070 used to generate cDNA; from this, segments of the genes indicated at the left were

49

1071   amplified using the primers listed in Data Set S2, Sheet 5, and the products were

1072   analyzed by agarose gel electrophoresis. Fragment sizes (in bp) are indicated at right

1073   and the ladder bands shown are 400, 500, 650, 850 and 1000 bp for the top panel; 200,

1074   300, 400, 500, and 650 bp for the middle panel; and 100, 200, and 300 bp for the bottom

1075   panel. C. Quantitative analysis of *PDR802* expression. Samples of RNA isolated as in B

1076   were analyzed for *PDR802* expression by qRT-PCR. All results were normalized to *ACT1*

1077   expression. Each symbol represents a biological replicate, with the mean and standard

1078   deviation also shown. ***, $p<0.001$ compared to KN99α by one-way ANOVA with posthoc

1079   Dunnett test.

1080

1081   **Figure S2. Organ burdens.** A. Mean +/- SD values of total colony-forming units (CFU) in

1082   the indicated tissue of mice from the Figure 1 survival curve are shown. Each point is the

1083   average value for a single animal at the time of death. For *pdr802* infections, red circles

1084   represent mice sacrificed at days 65 and 69, while blue circles represent mice sacrificed

1085   at the end of the study (day 100). B. Mean +/- SD of total colony-forming units (CFU) in

1086   the blood and brain at the indicated times post-infection. C. Mean +/- SD of total colony-

1087   forming units (CFU) in the lung, blood and brain 75 days after infection with *pdr802*. Each

1088   color represents one mouse.

1089

1090   **Figure S3. Characterization of *pdr802* cells.** *Panels A-C.*10-fold serial dilutions of WT,

1091   *pdr802*, and *PDR802* cells were plated on the media shown and incubated at 30°C (A),

1092   37°C (B), or 37°C in the presence of 5% CO_2 (C). Nitrosative ($NaNO_2$) and oxidative

1093   (H_2O_2) stress plates were prepared with YNB medium and melanization plates containing

1094   L-DOPA were prepared as in the Methods; all other plates were prepared with YPD

1095   medium. *lac1*, a control strain lacking the ability to melanize (88). D. Urease activity of the

1096   indicated strains was evaluated using Christensen's urea solid medium (see Methods) at

1097   the indicated temperatures. *ure1*, a control strain that does not produce urease (17).

1098

1099   **Figure S4. Growth curves and capsule shedding.** *Panels A-B*. Growth of the strains

1100   indicated in YPD at 30°C (A) or DMEM at 37°C and 5% CO_2 (B) was assessed by

1101 OD_{600nm} at the times shown. C. Conditioned medium from the indicated strains was

1102   probed for the presence of GXM after growth in DMEM for 24 or 48 hours. Equal volumes

1103   of culture supernatant were analyzed without normalization to cell density.

1104   Immunoblotting was performed using the anti-GXM monoclonal antibody 302.

1105

1106   **Figure S5. Semi-automated assay for cryptococcal capsule imaging.** A. Schematic

1107   of applying this method to cryptococcal cells induced to form capsule by growth in DMEM

1108   (37°C, 5% CO_2) for 24 h, followed by cell wall and capsule staining. Thousands of cells

1109   may be imaged per well and analyzed automatically with software that annotates and

1110   measures the capsule (annotated on the micrograph in blue) and cell wall (annotated in

1111   bright green). See Methods for details. B. Capsule size distribution of WT cells after

1112   induction. Capsule thickness for each cell is the difference between the paired diameters

1113   of the cell wall and capsule, which is plotted here with reference to the mean value. C

1114   and D. Mean and SD (C) and cumulative percentage (D) analysis of WT compared to

1115   hyper and hypocapsular control strains (here *pkr1* and *ada2*, respectively). Capsule

1116   thickness is in arbitrary units, related to the pixels measured. E. The time required to

51

1117   analyze the capsule thickness of 1,000 cells by this method compared to manual

1118   assessment of India ink images.

1119

1120   **Figure S6. *PDR802* deletion induces Titan cell formation.** Mean +/- SD of (A) total cell

1121   diameter and (B) the ratio of total cell to cell body diameters (diameter ratio), assessed by

1122   measuring at least 50 cells per strain with ImageJ. **, $p<0.01$ and ****, $p<0.0001$ for

1123   comparison of *pdr802* to KN99α or *PDR802* by one-way ANOVA with posthoc Dunnett

1124   test for each day post-infection. C. Percent of Titan cells in the indicated strain, evaluated

1125   using various published parameters: cell body diameter above 10 or 15 µm (20) or total

1126   cell diameter above 30 µm (43).

1127

1128   **Figure S7. Pdr802 strain viability, putative DNA-binding motifs, and self-regulation.**

1129   A. The indicated strains were grown in DMEM at 37°C and 5% CO_2 for the times shown

1130   and samples were tested for their ability to form colonies on YPD medium. Plotted is the

1131   fold-change in CFU relative to the initial culture. B. Putative Pdr802-binding motifs

1132   determined using DREME (74). Primary and secondary hits are shown for analysis of

1133   1,000 bp upstream of the initiating ATG. C. Pdr802 self-regulation. The ratios (log_2) of

1134   reads from immunoprecipitated (IP) DNA to reads from input DNA were calculated for

1135   1,000 bp upstream of the first coding nucleotide (+1) of *PDR802*; shown is the difference

1136   in these values between tagged and untagged strains. Red triangles, complete Pdr802

1137   DNA-binding motifs (Figure S7B); blue triangles, partial motifs.

1138

52

1139   **Data Set S1. Pdr802 ChIP-Seq, RNA-Seq, and Dual-Threshold Optimization (DTO)**

1140   **data.** Sheet 1, peaks that occur in gene promoter regions that showed ≥2-fold enrichment

1141   when Chip-Seq was performed on strains expressing tagged versus untagged Pdr802,

1142   with annotation. Sheet 2, ChIP-Seq primary data of Pdr802-specific peaks. Sheet 3,

1143   RNA-Seq data. Sheet 4, DTO filtered data. Sheet 5, DTO primary data. Sheet 6, ChIP-

1144   Seq data of all peaks in mCherry-Pdr802 samples. Sheet 7, ChIP-Seq data of all peaks in

1145   untagged (WT) control samples.

1146

1147   **Data Set S2. Pdr802 target analysis and primers used in this study.** Sheet 1, Pdr802

1148   regulated genes that are down-regulated during Titan cell formation *in vitro* (48). Sheet 2,

1149   Pdr802 regulated genes that are up-regulated during Titan cell formation *in vitro* (48).

1150   Sheet 3, targets regulated by Pdr802 that are also dephosphorylated by calcineurin (63).

1151   Sheet 4, the intersection of Pdr802 targets and genes that are Crz1-independent

1152   calcineurin targets under conditions thermal stress (55). Sheet 6, primers used in this

1153   study. Fold enrichment and adjusted p (q) values throughout are for the DTO results.

1154

1155   **Supplementary Methods.**

Table 1. Pdr802 targets involved in quorum sensing and Titan cell formation.

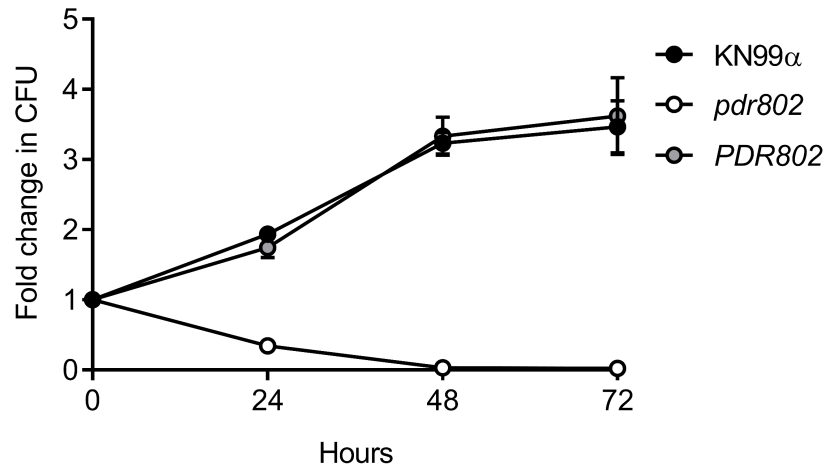| Biological process	CNAG	Gene name	ChIP-seq[1]	RNA-seq[2]	Description
Quorum sensing	00150	PQP1	1.38	-0.78	Peptidase
	03013	OPT1	1.25	-0.55	OPT small oligopeptide transporter
Titan cell formation	05835	LIV3	1.52	-0.84	Transcription factor
	05785	STB4	3.33	-1.71	Transcription factor
	05940	ZFC3/CQS2	2.23	0.68	Transcription factor

[1]Fold-change for mCherry-Pdr802 compared to WT

[2]Log$_2$ fold-change for pdr802 compared to WT

Table 2. Genes regulated by Pdr802 involved in adaptation to the host environment.

Biological process	CNAG	Gene name	ChIP-seq[1]	RNA-seq[2]	Description
Oxidative stress resistance	04981	CAT1	1.47	-1.60	Catalase 1
	05256	CAT2	1.41	-0.42	Catalase 2
	01019	SOD1	2.59	-0.53	Superoxide dismutase [Cu-Zn]
	00896	FZC34	2.22	-0.82	Transcription factor
	06327	MIG1	1.72	-0.78	DNA-binding protein creA
	00556	CCK1	1.78	-0.48	Casein kinase I
Melanin and cell wall formation	03202	CAC1	1.60	-0.61	Adenylate cyclase
	01845	PKC1	2.00	-0.48	AGC/PKC protein kinase
	07724	CUF1	1.27	-0.67	Metal-binding regulatory protein
	00740	SNF5	1.28	-0.70	Swi/snf chromatin-remodeling subunit
	01239	CDA3	2.63	1.08	Chitin deacetylase 3
	01230	MP98	2.74	0.96	Chitin deacetylase 2
	00776	MP88	1.86	1.23	Immunoreactive mannoprotein
Growth at 37°C	00405	KIC1	1.88	-0.97	Ste/ste20/ysk protein kinase
	03670	IRE1	1.66	-1.14	IRE protein kinase
Urease activity	07448	DUR3	2.13	-3.05	Urea transporter
	01209	FAB1	2.29	-0.49	1-phosphatidylinositol-3-P 5-kinase
	01938	KIN1	1.61	-0.34	CAMK/CAMKL/KIN1 protein kinase
	01155	GUT1	2.96	0.62	Glycerol kinase
	00791	HLH1	1.71	-1.09	Transcription factor
Capsule thickness	02802	ARG2	1.56	-0.59	Inositol/phosphatidylinositol kinase
	06809	IKS1	2.28	-0.44	IKS protein kinase
	01905	KSP1	2.02	-0.64	Serine/threonine protein kinase
	02877	FZC51	1.75	-0.69	Transcription factor
	07470	PDE2	2.42	-1.80	High-affinity phosphodiesterase
	03346	BZP4	3.52	1.30	Transcription factor
Calcineurin signaling	00156	CRZ1	1.44	-0.49	Transcription factor
	01744	HAD1	2.26	0.47	Phosphatase

[1]Fold-change for mCherry-Pdr802 compared to WT
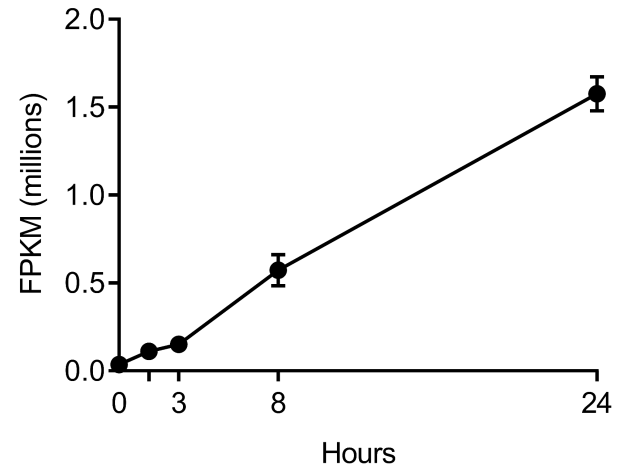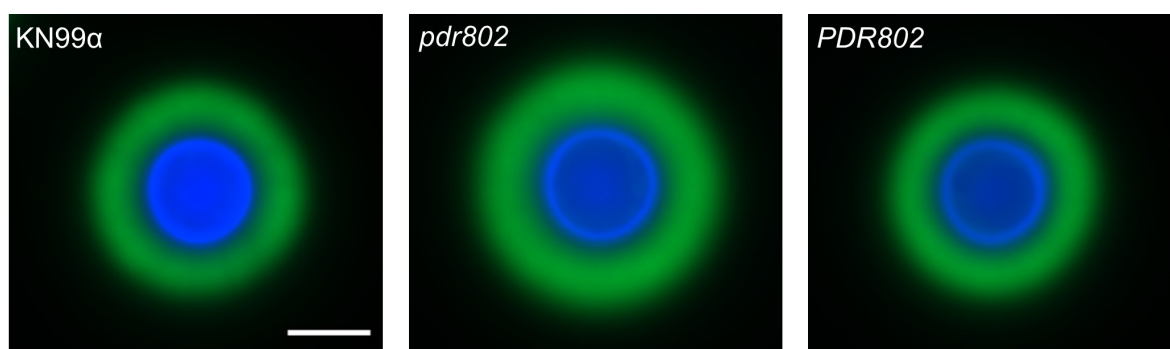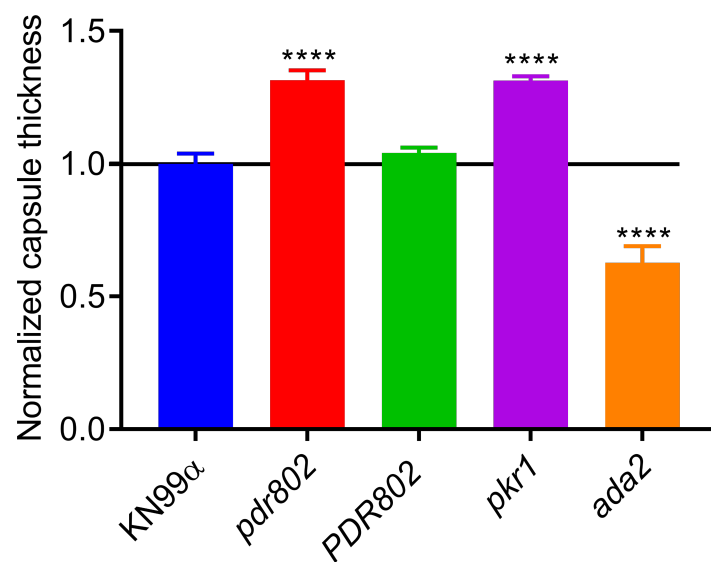
[2]$\log_2$ fold-change for *pdr802* compared to WT

FIGURE 1

FIGURE 2

FIGURE 3

FIGURE 4

FIGURE 5

FIGURE 6

FIGURE 7

FIGURE 8

FIGURE 9